CHAPTER I

INTRODUCTION: INTERSUBBAND STIMULATED EMISSION

A strong current injection exclusively into the upper subband of optically active multiple-quantum-well tunneling regions provides in the quantum cascade laser[1,2,3] a finite population inversion and actual lasing at mid-infrared frequency $\omega_\Delta \approx$ 300 meV. This seminal achievement culminates a quest for such intersubband stimulated emission which began in 1971 with a theoretical treatment by Drs. Kazarinov and Suris[4] soon after the seminal work on superlattices by Esaki and Tsu.[5]

The frequency ω_Δ of the stimulated emission is given by the level (or subband) separation, Δ, in the tunneling regions of the quantum cascade laser.[1,2,3] A simple modification of the tunneling potential thus allows the (stimulated) intersubband emission to be tuned anywhere within the mid-infrared and down to the far-infrared (or Tera-Hertz) regime. This tunability has been demonstrated by the recent observation[6] of spontaneous emission in such a quantum-cascade-laser design also at $\omega \approx 120$ meV.

There is a considerable interest in achieving such intersubband stimulated emission also in the far-infrared (or Tera-Hertz) regime, which we shall defines as frequencies $\omega \lesssim 10$ meV. There is a wealth of recent and exciting experimental results involving Tera-Hertz radiation and we mention in particular the observation of spontaneous emission in superlattices excited by a strong nonequilibrium current flow,[7,8] of coherent oscillations, or quantum beats, in optically excited double-quantum-well structures,[9,10] of Bloch oscillations[11,12] and photon-assisted tunneling[13] in superlattices, and finially of dynamical screening effects in resonant-harmonic generation in a double-quantum-well structure.[14]

In this dissertation we adapt the quantum-cascade-laser design[1,2,3] and consider theoretically the intersubband decay and resulting population inversion in a double-quantum-well tunneling structure with the *far-infrared* subband separation, $\Delta \approx 11$ meV. One may imagine this structure serves as an optically active region of a hypothetical far-infrared quantum cascade laser, but we emphasize that the design of a good waveguide confinement will be difficult due to the long wavelength of the far-infrared radiation.

The *bottom* panel of Figure 1.1 shows schematics of hypothetical far-infrared quantum-cascade-laser design presently investigated. The tunneling structure comprises a central asymmetric double-quantum-well region surrounding by two moderately doped injector layers serving as emitter and collector leads. The quantum-well region confines (more than) two resonant level E_1 and E_2 with subband separation $\Delta = E_2 - E_1 \approx 11$ meV. The choice of this central region is motivated by the small intersubband decay, $1/\tau \lesssim 0.03$ meV at $T \leq 50$ K, *observed*[15] under weak optical pumping of the corresponding *isolated* double-quantum-well structure.[14,15] Similar vanishing intersubband decay rates has been reported for quantum-well structures with corresponding far-infrared subband separations, see for example Refs. 16,17.

FIGURE 1.1 Schematic of far-infrared optically active tunneling structure (bottom panel) *and* examples of the *nonequilibrium* electron-electron scattering Γ which dominates the intersubband decay. The hypothetical structure comprises, see *bottom* panel, a central $L_{QB} = 243$ Å wide tunneling region (based on asymmetric double-quantum-well structure investigated in Ref. 15) *surrounded* by the n-doped (left/right) emitter/collector lead with band-edge $\phi_{L/R}$ and chemical potential $\mu_{L/R}$. A moderate voltage drop $V \equiv (\mu_L - \mu_R)/e \sim 20$ mV ensures a current injection Γ_e, solid arrow, *exclusively* into upper resonant level E_2 and fast tunneling escape rates $\Gamma_{c1(2)}$, dashed-single(double)-dotted arrow, out from lower level E_1 (from E_2.) Lower panel shows tunneling potential, resonant levels (solid bars,) and wavefunctions $\Psi^s_{1,2}(x)$ at special voltage drop V_{sym} where the quantum-confined Stark effect[23] causes an avoided crossing in the subband separation $\Delta(V) \equiv E_2 - E_1 \geq 10.9$ meV and restores a near-exact wavefunction inversion symmetry:[24] $\Psi^s_{1(2)}(x_0 - x) \approx +(-)\Psi^s_{1(2)}(x - x_0)$ (where x_0 is the node of $\Psi^s_2(x)$.) For comparison the dashed bars shows positions of $E_{1,2}$ at $V = 0$. *The three pairs* of opposite transition arrows in the *top* panel illustrate the dominant decay of the current-injected upper-subband distribution (dotted dispersion curve,) namely the *nonequilibrium* scattering (Γ) between two upper-subband electrons which both decay to subband E_1. As indicated by the pair of solid arrows, the scattering Γ occurs with the characteristic momentum transfer $q_\Delta = \sqrt{2m_e^*\Delta}$ and on average with no energy transfer.

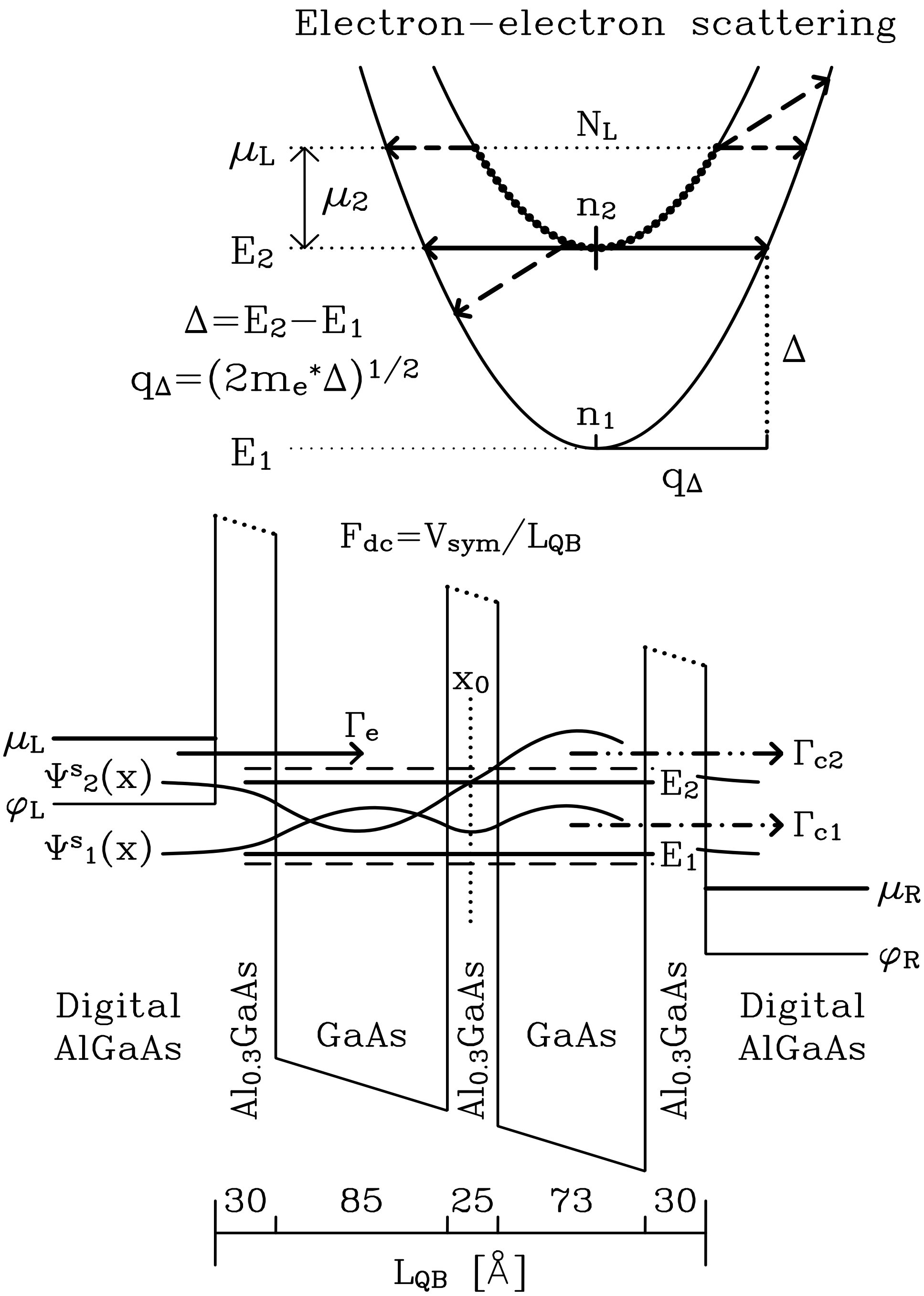

Electron−electron scattering
μ_L
μ_2
N_L
n_2
E_2
$\Delta = E_2 - E_1$
$q_\Delta = (2m_e{}^*\Delta)^{1/2}$
Δ
n_1
E_1
q_Δ
$F_{dc} = V_{sym}/L_{QB}$
x_0
μ_L
Γ_e
$\Psi^s{}_2(x)$
φ_L
$\Psi^s{}_1(x)$
Γ_{c2}
E_2
Γ_{c1}
E_1
μ_R
φ_R
Digital AlGaAs
$Al_{0.3}GaAs$
GaAs
$Al_{0.3}GaAs$
GaAs
$Al_{0.3}GaAs$
Digital AlGaAs
30
85
25
73
30
L_{QB} [Å]

FIGURE 1.1

Such vanishing intersubband decay rates are possible at temperatures $T \leq$ 50 meV because the optical phonon frequency ($\Omega_{LO} \approx 36$ meV in GaAs) *exceeds* the subband separation, $\Omega_{LO} > \Delta$. The optical-phonon emission is thus thermally activated with activation energy[15] $\Omega_{LO} - \Delta \approx 25$ meV.

We may assume that the experimental value, $1/\tau \leq 0.03$ meV at $T \leq 50$ K (observed[15] at weak optical pumping) constitute an approximate bound on the total single-electron decay,* Γ_{se}, resulting with the strong current injection exclusively into the upper-subband of the Figure 1.1 tunneling structure.

We demonstrate that it straight forward to ensure intersubband population inversion if the intersubband decay was limited to Γ_{se}. However, we find that the current injection results in a very significant *nonequilibrium* electron-electron scattering ($\Gamma \equiv \Gamma_{22\to 11}$ and $\Gamma_{22\to 21}$) which we evaluate for a complete upper-subband occupation below the emitter chemical potential.

The *top* panel of Fig. 1.1 illustrate typical intersubband scattering events contributing to Γ. Such processes involves two upper-subband electrons which both decay to the lower subband. This *nonequilibrium* scattering Γ is given by an intersubband Coulomb matrix element which can be determined from existing measurements[15] of a large equilibrium depolarization shift,[18,19,20,21,22] $\Delta^* - \Delta \approx$ 2 meV, of the absorption peak, Δ^*, from the subband separation, $\Delta \approx 11$ meV.

In addition there is the nonequilibrium electron-electron scattering $\Gamma_{22\to 12}$ which also involves two upper-subband electrons but where only one electron decays

* We define the total single-electron decay, Γ_{se} as the intersubband decay resulting from everything but the electron-electron interaction. That is, we define Γ_{se} as the intersubband decay resulting from impurity, interface-defect, acoustic-phonon scattering and from the thermally activated optical-phonon emission.

to the lower subband. This scattering is given by an intersubband Coulomb matrix element which we find essentially vanishes when, at a finite voltage drop, the so-called quantum-confined Stark effect[23] restores an approximate wavefunction-inversion symmetry.[24]

We demonstrate that the nonequilibrium electron-electron intersubband scattering Γ ($\Gamma_{22\to 21}$) is never significantly reduced by screening, and, unlike the near-equilibrium electron-electron scattering,[27,28] is *not* (only partially) inhibited by Pauli exclusion, as we can assume population inversion and hence a vanishing lower-subband occupation.

Furthermore, in this dissertation we (1) identify a simple scaling of scattering rate Γ with upper-subband occupation, (2) predict a very strong intersubband decay $\sim 2\Gamma \approx 10$ meV for an upper-subband sheet-density $N_L \approx 10^{11}$ cm^{-2} comparable to that in the mid-infrared quantum cascade laser,[1,3] (3) demonstrate that a smaller population inversion density ($\sim 0.25 \times 10^{11}$ cm^{-2}) *can* be maintained at a moderate tunneling current density, and finally (4) predict, also for the combined nonequilibrium electron-electron intersubband decay rate, $2\Gamma + \Gamma_{22\to 21}$, a dramatic bias dependence arising from the quantum-confined Stark effect.[23]

Finally we note that the predicted strong nonequilibrium electron-electron intersubband scattering is relevant also for the study of possibility of continuous-wave Bloch oscillations in double-quantum-well resonant-tunneling structures as has recently been addressed in two theory studies:[25,26] the strong electron-electron scattering may reduce the intersubband population inversion which is proportional[26] to the predicted net stimulated emission of such Bloch oscillations.

I.A Detailed overview of dissertation

Here in Chapter I, we briefly discuss the resonant current flow both in the standard double-barrier resonant-tunneling diode,[5,29,30,31] and in the two-level tunneling structure shown in Fig. 1. Specifically, we introduce simple rate equations to describe the current flow and demonstrate that population inversion requires that the tunneling escape rates out from the lower level *exceeds* the (nonradiative) intersubband decay. We estimate the tunneling rates into and out from the quasi-bound resonant levels for the potential shown in Figure 1.1 and demonstrate that it is straight forward to maintain a finite population inversion if the intersubband decay is limited to the total *single-electron* decay, Γ_{sp} (approximately bounded by the experimental value, $1/\tau \approx 0.03$ meV.) Finally, we explain how even a moderate *intersubband* population inversion may result in a significant stimulated emission because (a) the optical transitions is concentrated around a single frequency ω_Δ given by the subband separation Δ, and (b) the quantum-well potential results in very large optical transition matrix elements.

In Chapter II, we discuss the mid-infrared Quantum Cascade Laser following Refs. 1,2,3. We describe the chemical composition and corresponding effective tunneling potential. In particular we discuss the current injection in the set of 25 active tunneling regions separated by interjacent so-called injector layers serving as emitter and collector leads. We also describe the total current flow and power dissipation at threshold conditions, that is, just before the onset of lasing. Moreover, we explain a simple theory estimate[3] of the so-called (peak) material gain, i.e., the net amplification of the lasing mode if traveling *exclusively* within an (infinite) superlattice of the optically active regions with interjacent injector layers/leads. Finally, we explain how Capasso and coworkers achieved a good waveguide confinement by surrounding the optically active 25-period superlattice by so-called cladding layers with a smaller index of refraction.[3] This waveguide confinement both enhances the lasing intensity inside the optically active superlattice and prevents a potentially significant (impurity aided) free-carrier and plasmon reabsorption especially at the contact layers.

In Chapter III, we discuss the hypothetical far-infrared quantum-cascade-laser design in greater detail. We specify a possible chemical potential and describe the resulting potential as a function of the voltage drop V applied across the tunneling region. We determine the corresponding variation of the resonant levels and in particular identify an avoided crossing in the subband separation at voltage drop $V_{sym} = 22.9$ mV with potential shown in Figure 1.1. We also estimate the voltage-drop variation of the tunneling rates and estimate the range of voltage drops which ensures a current injection exclusively into the upper subband of the hypothetical tunneling structure. Moreover, we demonstrate that the voltage drop V_{sym} restores a near-exact wavefunction inversion symmetry in the still asymmetric potential. We determine the voltage-drop variation on this wavefunction-inversion symmetry and explain this quantum-confined Stark effect[23,24] within a simple two-level model. Finally, we discuss the total single-electron intersubband decay rate, Γ_{se}, which we, at temperatures $T \leq 25$ K, can assume bounded by the experimental value,[15] $1/\tau \approx 0.03$ meV.

In Chapter IV we provide a detailed study of the *nonequilibrium* electron-electron intersubband scattering $\Gamma \equiv \Gamma_{22\to11}$ ($\Gamma_{22\to12}$) between two upper subband electrons which both decay (of which only one decays) to the lower subband. We evaluate these nonequilibrium rates for a complete upper subband occupation below emitter chemical potential. We describe the effective Coulomb intersubband interaction and observe that this interaction (a) exhibits only a moderate variation with in the in-plane momentum transfer q and (b) shows only a correspondingly moderate dependence on an effective Thomas-Fermi screening wavevector q_{TF}. We furthermore find that the nonequilibrium scattering Γ is characterized by a matrix elements whose value at $q = 0$ can be extracted directly from the experimental observation[14,15] of a significant equilibrium depolarization shift.[19] Moreover, we identify a simple scaling of the scattering rate Γ with the upper-subband occupation. In contrast, we find no scaling for the other nonequilibrium scattering, $\Gamma_{22\to21}$, when (at a finite occupation) the Pauli exclusion principle begins to restrict the availability of final upper-subband states.

We furthermore predict a significant wavefunction-symmetry variation of both Γ and $\Gamma_{22\to21}$, and also of the combined electron-electron intersubband decay rate, $2\Gamma+\Gamma_{22\to21}$. We find that a very strong intersubband decay rate, $\sim 2\Gamma \sim 1.0$ meV, prevents an upper-subband occupation density $n_2 \approx 10^{11}$ cm^{-2}. Nevertheless, we demonstrate that a smaller finite intersubband population inversion, $\sim 0.25 \times 10^{11}$ cm^{-2} *can* be maintained at a current density comparable with the current density of the mid-infrared quantum cascade laser.[1,3]

In our concluding Chapter V we summarize our results and list of open questions. In particular, we observe that while a finite intersubband population can be maintained it does not guarantee that actual far-infrared lasing can be achieved. Especially the design of a good waveguide confinement of a potentially far-infrared lasing mode will be very difficult due to the very long wavelength.

Finally, in Appendix A we provide a formal derivation of the intersubband electron-electron scattering rates based on the Fermi golden rule. In particular, we demonstrate that the so-called direct and exchange contributions to the same-spin scattering cancel if the q-variation of intersubband Coulomb matrix element can be ignored. For the dominant opposite-spin scattering we derive the estimates evaluated in Chapter IV.

I.B The resonant-tunneling current flow

The standard resonant-tunneling diode comprises (for example) a central GaAs quantum-well layer separated from two outside n-doped GaAs leads by a pair of AlGaAs tunneling-barriers. As schematically illustrated in the upper panel of Fig. 1.2, this variation of the chemical composition defines an effective double-barrier potential for the conduction-band electrons and the higher potential in the AlGaAs-barrier layers traps a resonant level E_r in the central quantum-well. A typical width, 30–40 Å, of each barrier ensures a vanishing probability for tunneling from emitter to collector *unless* the electron energy matches that of the quasibound resonant level.

In the sample structure illustrated in Fig. 1.2, the resonant level E_r is in equilibrium (*top* panel) located well above the chemical potential of the leads, $E_r > \mu_L = \mu_R$. However, as illustrated in the *bottom* panel of Fig. 1.2, a finite voltage drop V applied across the tunneling region raises (lowers) the emitter (collector) Fermi sea and will result in a fast current injection rate, Γ_e, (tunneling escape rate, Γ_c,) when the quasibound level is positioned *between* the emitter

FIGURE 1.2 Schematic band profile of a resonant-tunneling heterostructure diode in equilibrium (upper panel) and under resonant operating conditions (lower panel.) The effective double-barrier potential traps a quasibound resonant level E_r between the emitter ('L') and collector ('R') leads with lower conduction band edge $\phi_{L/R}$ and chemical potential $\mu_{L/R}$. In Equilibrium, as illustrated in the *upper* panel, the resonant level is typically located above the chemical potential, $\mu_L = \mu_R$, and there is only a small linear-response conductivity. However, as illustrated in the *lower* panel, a finite applied bias raises (lowers) the emitter (collector) lead. Under these so-called resonant conditions the quasibound level is positioned within the emitter Fermi sea, $\mu_L > E_r > \phi_L$, and there is both a large resonant-tunneling current injection, Γ_e, from the emitter into the quasibound level and a large tunneling escape rate, Γ_c, from the resonant level out to the collector lead. The resulting resonant-tunneling current flow is proportional to the steady-state nonequilibrium occupation of the resonant level, E_r.

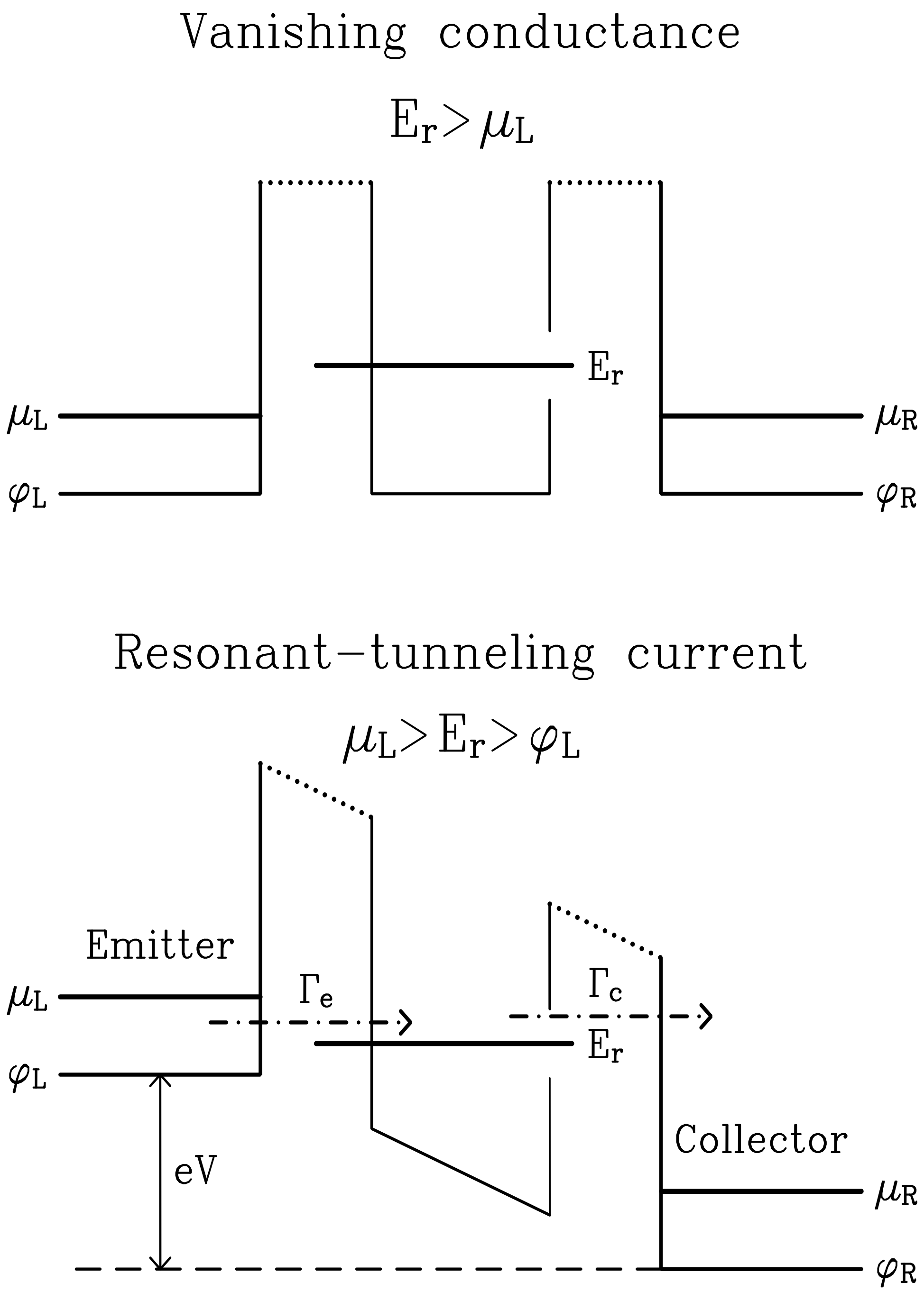
Vanishing conductance
E_r > μ_L
E_r
μ_L
φ_L
μ_R
φ_R
Resonant–tunneling current
μ_L > E_r > φ_L
Emitter
Γ_e
Γ_c
E_r
μ_L
φ_L
eV
Collector
μ_R
φ_R

FIGURE 1.2

band-edge and chemical potential (above the collector chemical potential,)

$$\phi_L < E_r < \mu_L, \tag{1}$$

$$(E_r > \mu_R.) \tag{2}$$

A significant current may flow under the resonant conditions, Eqs. (1) and (2), because the quasi-bound resonant level can be exploited by a finite (two-dimensional) density of electrons, which, in effect, tunnel in parallel. The electrons are free to move in the plane of the heterostructure, that is, perpendicular to the tunneling current flow. This motion can be characterized in-plane momentum $\vec{k}$ and dispersion

$$E_r + E_{||}(k) \equiv E_r + \frac{k^2}{2m_e^*}, \tag{3}$$

given by the effective electron mass m_e^*. All such subband states with an energy, Eq. (3), below the emitter chemical potential, μ_L, will contribute to the current flow. With just a moderate doping concentration, $\sim 10^{17}$ cm^{-3}, giving a $\mu_{L/R} - \phi_{L/R} \sim$ 10 meV thickness of the emitter/collector Fermi sea, on can obtain a finite density of subband states,

$$N_L = \frac{2m_e^*(E_r - \phi_L)}{2\pi} \sim 10^{11} \text{ cm}^{-2}. \tag{4}$$

Under resonant conditions, Eqs. (1) and (2), the resulting current flow can be determined by a simple rate equation[32] for the electron occupation density, n, of the resonant level. Specifically, since all subband states below the emitter chemical potential may tunnel in parallel, we have

$$\frac{dn}{dt} = (N_L - n)\Gamma_e - n\Gamma_c. \tag{5}$$

The steady-state solution, $n^0 = N_L\Gamma_e/(\Gamma_e + \Gamma_c)$ (limited by N_L,) of Eq. (5) then yields the current flow

$$J = e\Gamma_e(N_L - n^0) = e\frac{\Gamma_e\Gamma_c}{\Gamma_e + \Gamma_c}. \tag{6}$$

The discussion of the resonant-tunneling current flow is thus reduced to a determination of the rates Γ_e and Γ_c, which, following Bardeen,[33] may be obtained by the Fermi golden rule.

Adapting the approach described in Refs. 33, 34 we provide below a formal Fermi-golden-rule estimate for the tunneling rates as follows. We assume a simple voltage-drop dependence, $\phi_{L/R}(V) = \phi_{L/R}(V = 0) + / - eV/2$, for the position of the emitter/collector lower band edge, exactly as illustrated in both Figure 1.1 and Figure 1.2, and express all energies from the position of the GaAs quantum-well potential at $V = 0$. For simplicity we also assume that the potential confining quasi-bound resonant level E_r can be treated as symmetric and ignore the changes in the barrier potential ϕ_B with the finite voltage-drop V. For an electron of energy $E \ll (\phi_B - E)$ we then obtain the probabilities, $T_L(E)$ and $T_R(E)$, for tunneling from the quantum-well region to the emitter ('L') and to collector ('R') leads as

$$T_L(E) \approx 16\Theta(E - \phi_L)\frac{\sqrt{E(E - \phi_L)}}{\phi_B - E}\exp(-2L_B\sqrt{2m_e^*(\phi_B - E}), \tag{7}$$

$$T_R(E) \approx 16\Theta(E - \phi_R)\frac{\sqrt{E(E - \phi_R)}}{\phi_B - E}\exp(-2L_B\sqrt{2m_e^*(\phi_B - E}), \tag{8}$$

where L_B denotes the barrier width.

The escape rate out from level E_r can be estimate as a product of the tunneling probability, given by Eq. (8), and a tunneling attempt frequency. The thickness, L_{QB}, of the tunneling region (introduced in Figure 1.1) represent a simple measure of the extension of the quasi-bound wavefunction in level E_r. Hence, we may estimate this tunneling attempt frequency[35,36] as the ratio of the resonant-level velocity $v_0 = \sqrt{2E_r/m_e^*}$ to $2L_{QB}$. Thus we finally obtain the estimate

$$\Gamma_e = \frac{v_0}{2L_{QB}} T_L(E_r) \equiv \frac{\sqrt{2E_r/m_e^*}}{2L_{QB}} T_L(E_r), \tag{9}$$

for the current injection rate and

$$\Gamma_c = \frac{v_0}{2L_{QB}} T_R(E_r) \equiv \frac{\sqrt{2E_r/m_e^*}}{2L_{QB}} T_R(E_r), \tag{10}$$

for the tunneling escape rate.

We emphasize that we have in Eqs. (8) and (10) only obtained a *qualitative* estimate of the tunneling escape rate, Γ_c. We have for example not included the effects on the tunneling potential on the barrier height, nor have we treated possible electron charging effects. However, such quantitative corrections to Γ_c (and Γ_e) can be offset by a change in the actual barrier thickness L_B which has a dramatic affect on the tunneling probability, see Eq. (8).

We also note that the above simple treatment based on the rate equation, Eq. (5), clearly suggest that the predicted current flow at resonant conditions, Eq. (1), is very robust toward scattering. It is in fact under these resonant conditions possible to derive the rate equation independently of the strength of an interaction at the resonant level, provided the in-plane momentum transfer can be ignored.[36]

The insensitivity toward scattering of the current flow at resonant conditions, Eq. (1) and (2), is in contrast to the situation in the so-called valley region of the current-voltage characteristics of a standard double-barrier resonant-tunneling diode. This valley region results at even higher voltage drops which pushes the emitter lower band edge ϕ_L above the level E_r. As is evident from the estimate, Eq. (9), we then have $\Gamma_e \equiv 0$ and we expect no current injection *directly* into the lower subband. When the resonant-tunneling diode enters this regions there is a dramatic drop in the current flow and a negative differential conductance is observed — a feature which has continued to sustain interest since its first observation in 1974.[29] Specifically, the negative differential conductance has possible application in the realization of very fast oscillations which should in principle be able to operate even at Tera-Hertz frequencies, i.e., in the far-infrared regime.

It has, however, proven difficult to prevent a small but finite inelastic tunneling also in the valley region. In particular a so-called phonon echo in the valley region has been identified with with electrons which emits an optical-phonon emission while tunneling.[30,31] Such inelastic resonant tunneling has been the focus of several theory investigations, see for example Refs. 37, 38, 39, 40, 41, 42, 43.

On the other hand, there *is* a large difference between the current flow at resonant conditions and in the valley current. Thus if, in a two-level resonant-tunneling structure, one can achieve both of the following conditions

$$\phi_L \leq E_2 \leq \mu_L, \tag{11}$$

$$\phi_L > E_1 > \mu_R, \tag{12}$$

one has at the same time a large current injection Γ_e into upper level E_2 *but* only an insignificant current injection into E_1. Moreover, the condition, $E_1 > \mu_R$, ensures a fast tunneling escape rate Γ_{c1} out from lower-level E_1 and the (almost) exclusive upper-subband current injection may then provide a finite intersubband population and far-infrared stimulated emission. This is particularly so in the

Figure 1.1 tunneling structure where achieving the conditions Eqs. (11) and (12) requires just a moderate voltage drop, $V \approx 12$–30 mV, and in particular the optical-phonon emission remains thermally activated.

I.C Intersubband population inversion in two-level tunneling structure

Figure 1.3 illustrate the (voltage-drop) dependent intersubband optical response of the Figure 1.1 two-level tunneling structure. The *top* panel shows the level positions, E_1 and E_2, and the emitter/collector Fermi sea (from lower band edge $\phi_{L/R}$ to chemical potential $\mu_{L/R}$,) in equilibrium where only the lower level E_1 is occupied. As indicated by the solid upwards arrow, the tunneling structure will in equilibrium provide a significant intersubband absorption.

However, as illustrated in the *bottom* panel of Figure 1.4, the Figure 1.1 tunneling structure requires just a moderate voltage drop ($V \gtrsim 12$ mV) to achieve the conditions, Eqs. (11) and (12), for the exclusive upper-subband current-injection. As we shall eventually demonstrate, the current injection may then maintain a finite population inversion in spite of a significant decay. As a consequence there will be a significant intersubband stimulated emission (indicated by the solid downward arrow) at a frequency ω_Δ given by the subband separation $\Delta = E_2 - E_1$.

The bottom two panels of Figure 1.4 illustrate the scattering processes contributing to the total nonradiative* intersubband decay γ_{nr}. In particular the solid arrow in the *bottom left* panel illustrates the elastic impurity and interface-defect

* We consider the quantum-cascade-laser design in the absence of any external radiation and in particular below a possible threshold condition.

FIGURE 1.3 Schematics of intersubband optical response of the two-level resonant-tunneling structure shown in Figure 1.1. The *top* panel illustrate the equilibrium situation. Only the lower level (with equilibrium position E_1^0) is then occupied and the system exhibits a resonantly enhanced absorption (solid upward arrow) at a frequency given by the equilibrium subband separation $\Delta(V=0) = E_2^0 - E_1^0$. The *bottom* panel illustrate that it takes only a moderate voltage drop ($V \gtrsim 12$ mV) to position the upper level within the emitter Fermi sea, $\phi_L < E_2 < \mu_L$, and the lower level below the emitter band edge but above the collector Fermi surface, $\phi_L > E_1 > \mu_R$. As a consequence there is then both an exclusive upper-subband current injection (left dashed-double-dotted arrow) and fast tunneling escape rates (right dashed-dotted arrows) out from both upper and lower resonant levels E_2 and E_1. The current injection may then provide a finite current population inversion which can result in a significant, resonantly enhanced, stimulated emission (solid downward arrow) at a frequency ω_Δ given by the subband separation $\Delta = E_2 - E_1$, see also top panel of Figure 1.4.

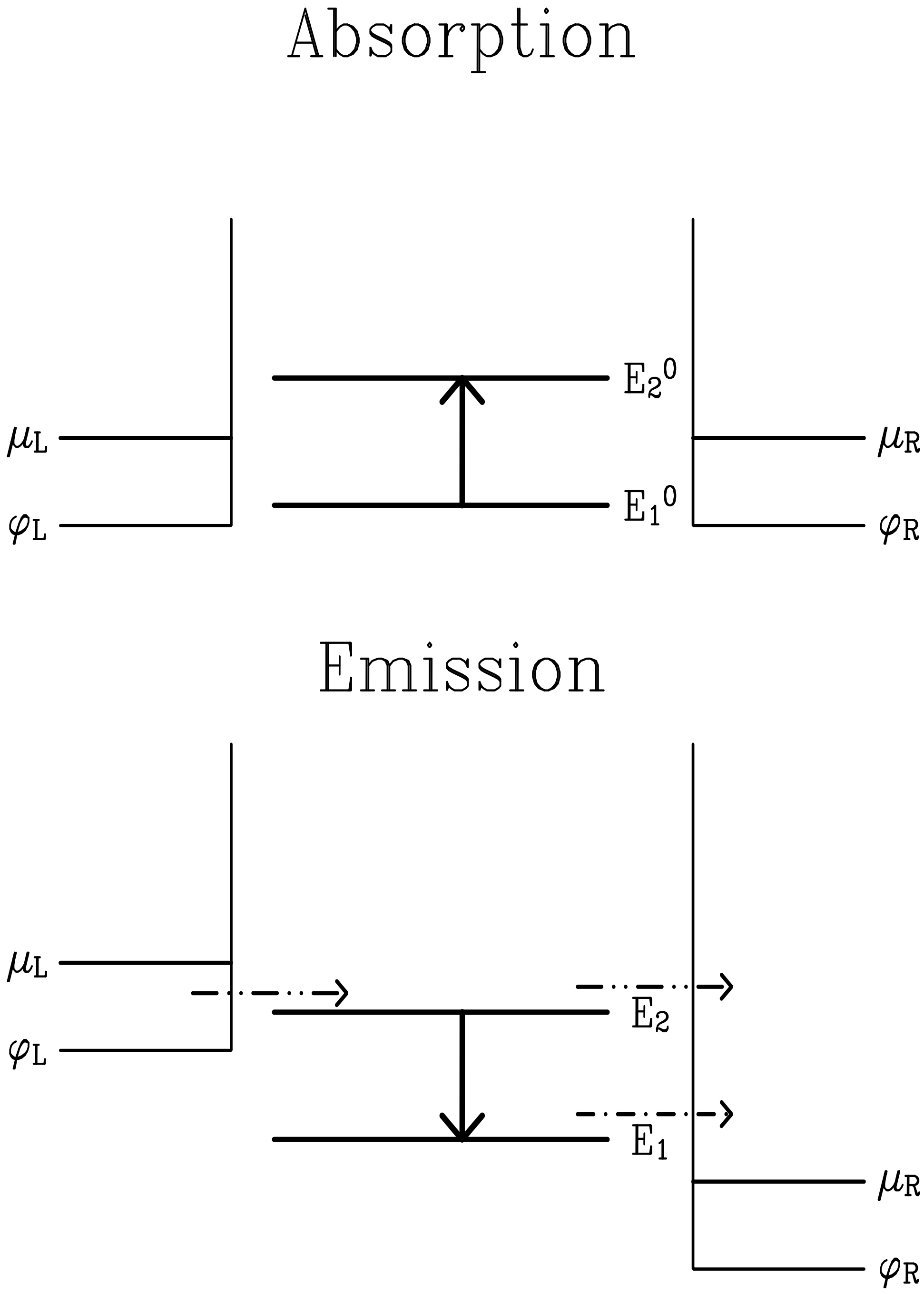
Absorption
μ_L
φ_L
E_2^0
E_1^0
μ_R
φ_R
Emission
μ_L
φ_L
E_2
E_1
μ_R
φ_R

FIGURE 1.3

FIGURE 1.4 Intersubband scattering event, *bottom two* panels, *and* resonantly enhanced intersubband stimulated emission with an exclusive upper-subband current injection, *top* panel. The solid arrow in the *bottom left* panel illustrate the intersubband decay due to impurity and interface defect scattering. The dashed-dotted arrow, also in the bottom left panel, illustrate that the decay due to acoustic-phonon can be considered as essentially elastic (the *actual* average energy transfer is ~ 0.5 meV $\ll \Delta$ and the panel shows a very exaggerated electron-acoustic-phonon energy-transfer for clarity.) The pair of opposite transition arrows in the *bottom right* panel illustrate the nonequilibrium electron-electron scattering (also illustrated in top panel of Figure 1.1.) Finally, the *top* panel explain why the *intersubband* optical transitions is resonantly enhanced around single frequency, $\omega_\Delta \sim \Delta$, because of the vanishing optical in-plane momentum transfer and because the subbands are described by parallel parabolae. It is, as a consequence, possible for a moderate upper-subband occupation density $\sim 10^{11}$ cm^{-2} (dotted dispersion curve,) injected (Γ_e) below emitter chemical potential μ_L, to provide a significant intersubband stimulated emission.

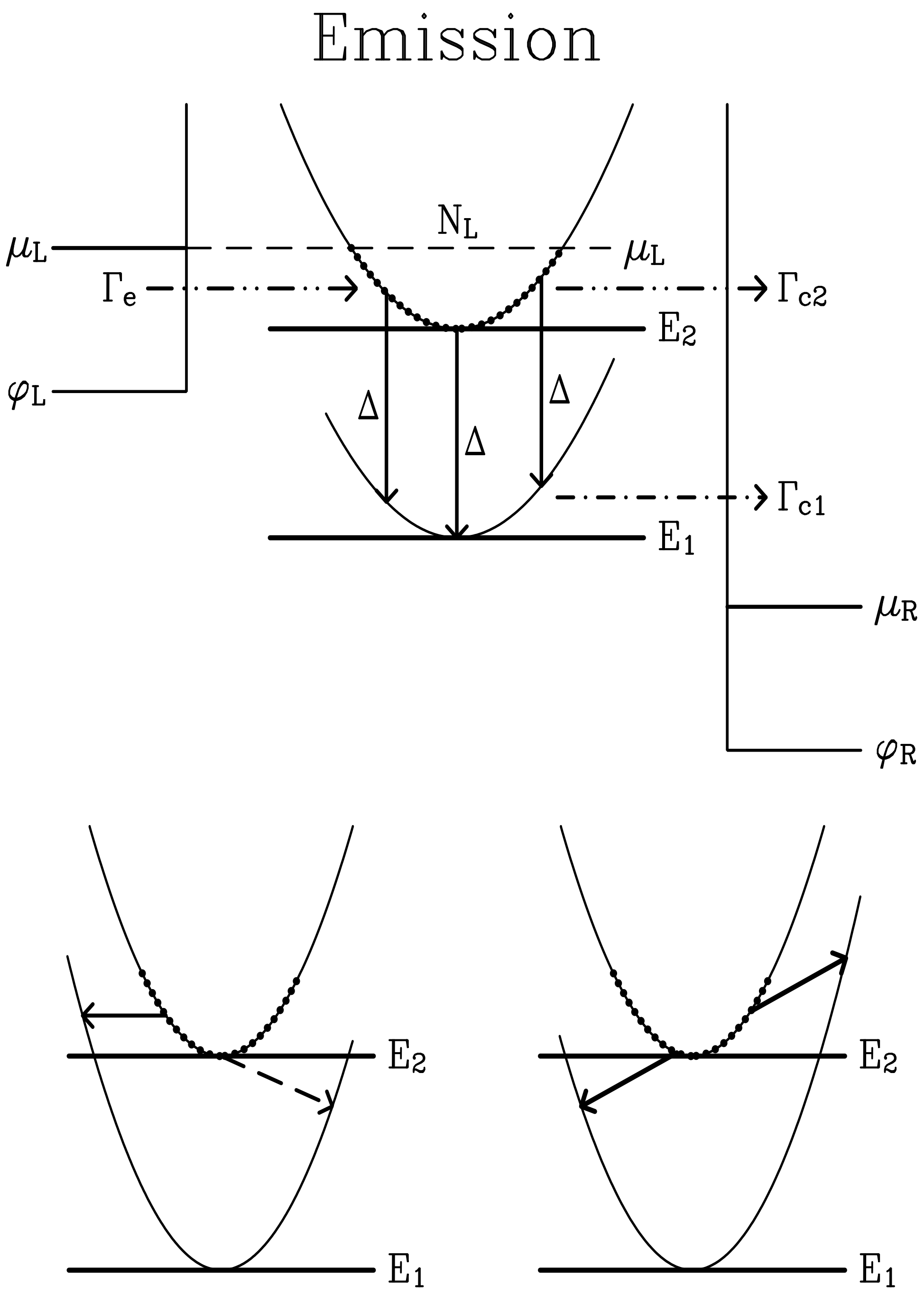
Emission
N_L
μ_L
μ_L
Γ_e
Γ_{c2}
E_2
φ_L
Δ
Δ
Δ
Γ_{c1}
E_1
μ_R
φ_R
E_2
E_1
E_2
E_1

FIGURE 1.4

scattering, the dashed arrow also in the *bottom left* panel illustrates the almost elastic electron acoustic-phonon scattering, and finally the pair of opposite solid transition arrows in the *lower right* panel illustrates a nonequilibrium electron-electron scattering event (also illustrated in the top panel of Figure 1.1.) This total nonradiative decay $\gamma_{nr} = \gamma_{nr}(n_2, n_1)$ will in general depend on the upper- and lower-subband occupation densities, n_2 and n_1.

Generalizing the rate equation, Eq. (5), we may estimate the resulting upper- and lower-subband occupation densities, n_2 and n_1, from the two-level rate equation

$$\frac{dn_2}{dt} = (N_L - n_2)\Gamma_e - n_2\Gamma_{c2} - \gamma_{nr}(n_1, n_2), \tag{13}$$

$$\frac{dn_1}{dt} = -n_1\Gamma_{c1} + \gamma_{nr}(n_1, n_2), \tag{14}$$

involving the total nonradiative decay γ_{nr}, the current injection rate Γ_e, and the tunneling escape rates Γ_{c1} and Γ_{c2} out from level E_1 and E_2, respectively. In this two-level rate equation the maximum upper-subband occupation density, N_L, is given by

$$N_L = \frac{2m_e^*(E_2 - \phi_L)}{2\pi} \sim 10^{11}\ \mathrm{cm}^{-2}, \tag{15}$$

in complete analogy with the single-level case, see Eq. (4).

Assuming first that the intersubband decay is linear in n_2, we introduce an intersubband decay rate, Γ_{nr}, defined by

$$\gamma_{nr} \equiv n_2\Gamma_{nr}. \tag{16}$$

Inserting this assumption in the two-level rate-equation, Eqs. (13) and (14), we find the steady-state occupation densities

$$n_2 = N_L\frac{\Gamma_e}{\Gamma_e + \Gamma_{c2} + \Gamma_{nr}}, \tag{17}$$

$$n_1 = N_L\frac{\Gamma_e\Gamma_{nr}}{(\Gamma_e + \Gamma_{c2} + \Gamma_{nr})\Gamma_{c1}}. \tag{18}$$

The resulting steady-state intersubband population inversion and current density are

$$\Delta n \equiv (n_2 - n_1) = n_2(1 - \frac{\Gamma_{nr}}{\Gamma_{c1}}), \tag{19}$$

$$J \equiv e\Gamma_e(N_L - n_2) = e\Gamma_e N_L \frac{\Gamma_{c2} + \Gamma_{nr}}{\Gamma_e + \Gamma_{c2} + \Gamma_{nr}}. \tag{20}$$

In particular, we observe that maintaining population inversion requires that the lower-level escape rate Γ_{c1} *exceeds* the intersubband decay rate Γ_{nr}.

For the potential shown in Figure 1.1 we estimate tunneling escape rates as follows. The voltage drop $V_{sym} = 22.9$ mV positions the upper (lower) quasi-bound-resonant level at $E_2 \approx 51$ meV ($E_1 \approx 40$ meV,) and the lower collector emitter at $\phi_L \approx 25$ meV (relative to the GaAs potential at $V = 0$.) Assuming a $L_B = 30$ Å ($\phi_B = 214$ meV) barrier width (barrier potential height) we estimate (from Eqs. (8) and (10)) the tunneling escape rates

$$\Gamma^s_{c2} \approx 1.0 \text{ meV}, \tag{21}$$

$$\Gamma^s_{c1} \approx 0.5 \text{ meV}. \tag{22}$$

If the total nonradiative decay rate Γ_{nr} was bounded by the recent experimental observation of just a small decay rate, $1/\tau \leq 0.03$ meV (at temperatures $T \leq 50$ K) it would be straight forward to maintain a finite population inversion $\gtrsim 10^{11}$ cm^{-2}. Unfortunately we find that the nonequilibrium current injection results in a very significant *nonequilibrium* electron-electron scattering which significantly reduces the resulting population inversion and which is the main focus of the dissertation.

I.D The intersubband stimulated emission

In this final section we discuss the resulting intersubband stimulated emission. In particular we explain how an intersubband population inversion of $\sim 10^{11}$ cm^{-2} can provide a significant stimulated emission because (a) the optical transitions occurs around a single frequency ω_Δ set by the subband separation $\Delta = E_2 - E_1$, and (b) the confinement within the quantum-well structure results in very large optical transition matrix elements.

For a detailed account of the intersubband stimulated emission it is necessary to again consider the electron motion parallel to the heterostructure layers, i.e., perpendicular to the current flow. In the absence of any scattering, this in-plane motion is independent of the electron tunneling and can be characterized by a (two-dimensional) momentum $\vec{k}$ and dispersion

$$E_{||}(\vec{k}) = \frac{k^2}{2m_e^*}. \tag{23}$$

Both the upper and lower level thus give rise to a subband of states

$$\langle x; \vec{\rho} | \Psi_{2(1)}; \vec{k} \rangle = \frac{1}{\sqrt{A}} e^{i\vec{k}\cdot\vec{\rho}} \Psi_{2(1)}(x) \tag{24}$$

with energies

$$E_{2(1)}(k) = E_{2(1)} + E_{||}(k), \tag{25}$$

illustrated by the pair of parabolae in the *top* panel of Fig. 1.4. We assume for simplicity that the fast lower-subband escape rate (Γ_{c1}) ensures a vanishing lower-subband occupation, whereas the exclusive upper-subband current injection (Γ_e) provides the finite upper-subband occupation (dotted dispersion curve in Figure 1.4) $n_2 = \Delta n \sim 10^{11}$ cm^{-2}.

The intersubband optical transitions are described by dipole matrix elements

$$\langle \Psi_1; \vec{k}_f | x | \Psi_2; \vec{k}_i \rangle = \delta_{\vec{k}_f, \vec{k}_i} \langle \Psi_1 | x | \Psi_2 \rangle, \tag{26}$$

$$\langle \Psi_1 | x | \Psi_2 \rangle \equiv \int \Psi_1(x) x \Psi_2(x) dx \tag{27}$$

with a vanishing in-plane momentum transfer. Hence, as illustrated by the set of downward optical transition arrows in Figure 1.4, *all* upper-subband electrons will contribute to the stimulated at a frequency $\omega_\Delta \sim \Delta$. This is in contrast with the standard inter-*band* semiconductor laser where the population inversion is distributed over a range of possible transition energies, see Refs. 44, 45.

In addition, the quantum-confinement provides very large numerical values of the optical transitions matrix elements, Eq. (27). In fact for the Figure 1.1 tunneling structure the quantum confinement results in a very significant oscillator strength,

$$f_{21} = 2m_e^* \Delta |\langle \Psi_2 | x | \Psi_1 \rangle|^2 \approx 0.46 \tag{28}$$

with dipole matrix element $\langle \Psi_2 | x | \Psi_1 \rangle \approx 50$ Å. A correspondingly large oscillator strength, and the fact that the optical transition is concentrated around one transition frequency, allows just a $\Delta n \sim 10^{11}$ cm^{-2} population inversion density in the mid-infrared quantum cascade laser[1,3,2] to provide a significant stimulated emission and actual lasing.

REFERENCES

1. J. Faist, F. Capasso, D. L. Sivco, C. Sirtori, A. L Hutchinson, and A. Y. Cho, *Science* **264**, 553 (1994).

2. J. Faist, F. Capasso, D. L. Sivco, C. Sirtori, A. L. Hutchinson, and A. Y. Cho, *Electronics Letters* **30**, 865–866 (1994).

3. J. Faist, F. Cappasso, D. L. Sivco, A. L. Hutchinson, C. Sirtori, S. N. G. Chu, and A. Cho, *Appl. Phys. Lett.* **65**, 2901 (1994).

4. R. F. Kazarinov and R. A. Suris, *Fiz. Tekh. Poluprovodn.* **5**, 797 (1971) [*Sov. Phys. Semicond.* **5**, 707 (1971)]; **6**, 148 (1972) [**6**, 120 (1972)].

5. L. Esaki and R. Tsu, *IBM J. Res. Dev.* **14**, 61 (1970).

6. C. Sirtori, F. Capasso, J. Faist, D. L. Sivco, A. L. Hutchinson, and A. Y. Cho, *Appl. Phys. Lett.* **66**, 4 (1995).

7. M. Helm, P. England, E. Colas, F. DeRosa, and S. J. Allen, Jr., *Phys. Rev. Lett.* **63**, 74 (1989).

8. S. J. Allen, G. Brozak, E. Colas, F. DeRosa, P. England, J. Harbison, M. Helm, L. Florez, and M. Leadbeater, *Semicond. Sci. Technol.* **7**, B1–B5 (1992).

9. S. Luryi, *Solid State Commun.* **65** 787 (1988).

10. H. G. Roskos, M. C. Nuss, J. Shah, K. Leo, D. A. B. Miller, A. M. Fox, S. Schmitt-Rink, and K. Köhler, *Phys. Rev. Lett.* **68**, 2216 (1992).

11. K. Leo, P. H. Bolivar, F. Brüggemann, R. Schwedler, and K. Köhler, *Solid State Commun.* **84**, 943 (1992).

12. C. Waschke, H. G. Roskos, R. Schwedler, K. Leo, H. Kurz, and K. Köhler, *Phys. Rev. Lett.* **70**, 3319 (1993).

13. P. S. S. Guimaraes, Brian J. Keay, Jann, P. Kaminski, and S. J. Allen, Jr., P. F. Hopkins and A. C. Gossard, L. T. Florez and J. P. Harbison, *Phys. Rev. Lett.* **70**, 3792 (1993).

14. J. N. Heyman, K. Craig, B. Galdrikian, M. S. Sherwin, K. Campman, P. F. Hopkins, S. Fafard, and A. C. Gossard, *Phys. Rev. Lett.* **72**, 2183 (1994).

15. J. N. Heyman, K. Unterrainer, K. Craig, B. Galdrikian, M. S. Sherwin, K. Campman, P. F. Hopkins, A. C. Gossard, To appear in *Phys. Rev. Lett.*.

16. K. Craig, C. L. Felix, J. N. Heyman, A. G. Markelz, J. P. Bergman, P. O. Holtz, B. Bonemar, K. Campman, J. L. Mertz, and A. C. Gossard, preprint, 1995.

17. C. I. Harris, T. Lundström, Q. X. Zhao, J. P. Bergman, P. O. Holtz, B. Bonemar, K. Campman, J. L. Mertz, and A. C. Gossard, preprint, 1995.

18. J. F. Ward, *Rev. Mod. Phys.* **37**, 1 (1965).

19. S. J. Allen, Jr., and D. C. Tsui, and B. Vinter, *Solid State Commun.* **20**, 425–428, (1976).

20. Tsuneya Ando, A. B. Fowler, and F. Stern, *Rev. Mod. Phys.* **54**, 437 (1982); see pp. 473–476.

21. Q. P. Li, S. Das Sarma, *Phys. Rev. B* **43**, 11768 (1991); Ben Yu-Kuang Hu and S. Das Sarma, *Phys. Rev. B* **48**, 5469 (1993).

22. M. Zaluzny, *Phys. Rev. B* **47**, 3995 (1993); *J. Appl. Phys.* **74**, 4716 (1993).

23. D. A. B. Miller, D. S. Chelma, T. C. Damen, A. C. Gossard, W. Weigmann, T. H. Wood, and C. A. Burrus, *Phys. Rev. Lett.* **53**, 2173 (1984).

24. Jerome Faist, Federico Capasso, Albert L. Hutchinson, Loren Pfeiffer, and Ken W. West, *Phys. Rev. Lett.* **71**, 3573 (1993). This paper reports and explains the corresponding voltage-drop variation of the optical selection rules.

25. S. A. Gurvitz, *Phys. Rev. B* **44**, 11924 (1991).

26. A. N. Korotkov, D. V. Averin, and K. K. Likharev, *Phys. Rev. B* **49**, 7548 (1994). This paper includes a treatment of the elastic scattering only.

27. V. I.Fal'ko, *Phys. Rev. B* **47**, 13585 (1993).

28. P. Sotirelis, *Phys. Rev. B* **47**, 12744 (1993).

29. L. L. Chang, L. Esaki and R. Tsu, *Appl. Phys. Lett.* **24**, 593 (1974).

30. V. J. Goldman, D. C. Tsui and J. E. Cunningham, *Phys. Rev. B* **36**, 7635 (1987).

31. M. L. Leadbeater, E. S. Alves, L. Eaves, M. Henini, O. H. Hughes, A. Celeste, J. C. Portal, G. Hill and M. A. Pate, *Phys. Rev. B* **39**, 3438 (1989).

32. S. Luryi, *Appl. Phys. Lett.* **47**, 490 (1985).

33. J. Bardeen, *Phys. Rev. Lett.* **6**, 57 (1961).

34. N. S. Wingreen, *Resonant tunneling with an electron-phonon interaction,* (Physics Dissertation, Cornell University, 1989,) pp. 51–55.

35. M. Jonson and A. Grincwajg, *Appl. Phys. Lett.* **51**, 1729 (1987).

36. J. H. Davies, S. Hershfield, P. Hyldgaard and J. W. Wilkins, *Phys. Rev. B* **47**, 4603 (1993).

37. L. I. Glazman and R. I. Shekhter, *Zh. Eksp. Teor. Fiz.* **94**, 292 (1988) [Sov. Phys. JETP **67**, 163 (1988)].

38. M. Jonson, *Phys. Rev. B* **39**, 5924 (1989).

39. N. S. Wingreen, K. W. Jacobsen and J. W. Wilkins, *Phys Rev. Lett.* **61**, 1396 (1988).

40. E. V. Anda and F. Flores, *J. Phys.: Condens. Matter* **3**, 9087 (1991).

41. R. Lake and S. Datta, *Phys. Rev. B* **45**, 6670 (1992).

42. C. H. Grein, E. Runge, and H. Ehrenreich, *Phys. Rev. B* **47**, 12590 (1993).

43. P. Hyldgaard, S. Hershfield, J. H. Davies, and J. W. Wilkins, *Annals of Physics* **236**, 1 (1994).

44. G. P. Agrawal and N. K. Dutta, *Semiconductor Lasers,* (Van Nostrand Reinhold, N. Y., 1993,) pp. 1–24.

45. P. S. Zory, *Quantum Well Lasers,* (Academic Press, Inc., Boston, 1993.)